CDRI ⟨◇⟩   UNDP

Global Infrastructure Resilience
Capturing the Resilience Dividend

**A new model for global
landslide susceptibility
assessment and
scenario-based hazard
assessment**
Norwegian Geotechnical Institute

Position Paper | 2023

NGI

A new model for global landslide susceptibility assessment and scenario-based hazard assessment

Farrokh Nadim, Rosa M. Palau, Eivind M. Paulsen, Erlend B. Storrøsten

Norwegian Geotechnical Institute, PO Box 3930 Ullevål Stadion, N-0806 Oslo, Norway

Abstract

This paper presents the approach to assess the global landslide hazard in the Global Infrastructure Resilience Index (GIRI) for the Biennial Global Infrastructure Resilience Report of the Coalition for Disaster Resilient Infrastructure (CDRI). The methodology involves integrating landslide susceptibility and earthquake characteristics or rainfall data to determine, on a global scale, the probability of earthquake- and precipitation-induced landslides. The latter is assessed for both present and future climate conditions. The susceptibility map categorises different terrains into five susceptibility classes, considering factors such as slope, vegetation (land use), lithology, and soil moisture, using global datasets. Rainfall information is gathered from the W5E5 dataset from 1979 to 2016 and the IPSL-CM6A-LR climate model from the ISIMIP3b dataset, covering the SSP126 and SSP585 scenarios for 2061-2100. To evaluate the potential for rainfall-triggered landslides, 24-hour rainfall intensities are utilised to classify areas into five rainfall hazard classes. The potential for earthquake-induced landslides is assessed based on the peak ground acceleration (PGA) of the earthquake event (scenario) at a given location and the susceptibility index of the terrain at that location. The landslide susceptibility map(s) and rainfall data or earthquake PGA are combined to produce a hazard matrix. The result is a probabilistic hazard map that can be used for scenario-based assessment of global landslide risk to critical infrastructure, with a resolution of three arc seconds (approximately 90 metres at the equator) for the globe.

Keywords: Landslides, rainfall-induced, earthquake-induced, climate change, hazard, global scale

1   Introduction

The term "landslide" refers to events involving gravity-driven, down-slope mass movement, like rockslides, debris flows, and slow-moving earth flows. Major landslides are often triggered by an extreme rainfall event, a strong earthquake or anthropogenic factors (human activity).

Rainfall- and earthquake-induced landslides represent an important hazard in mountainous regions worldwide. Landslides commonly impact the functioning of infrastructure assets such as roads and railways and occasionally damage buildings or result in fatalities (Petley 2012; Froude and Petley 2018). Precipitation-induced landslides are commonly triggered by short and intense rainfall events (Caine 1980; Guzzetti et al. 2008). As a consequence of climate change, the frequency and intensity of severe rainfall events that usually trigger landslides are expected to increase in some regions (Gariano and Guzzetti 2016). In addition, due to societal changes, tourism development, and the increased use of transport networks in mountain areas, the exposure of communities to landslides is growing in many parts of the world. Thus, understanding how the landslide hazard will change in future is crucial in planning mitigation measures along linear infrastructure and reducing the risk to the population. Earthquakes are another common triggering mechanism of landslides (e.g. Keefer 1984). Landslides triggered by strong earthquakes in mountainous areas often have catastrophic consequences. For example, about 25% of the 87,000 casualties (69,000 confirmed killed and 18,000 missing) caused by the Wenchuan Earthquake of 12 May 2008 were due to the landslides triggered by that event (Zhang et al. 2014).

Within the Natural Disaster Hotspots project (Dilley 2005; Nadim et al. 2006), landslide hazard maps were developed using global topography, lithology, earthquake and climate datasets to identify the most exposed countries. Subsequently, this approach was refined and improved and has been employed in various global (Nadim et al. 2013) and continental (Jaedicke et al. 2014) studies, including the Global Assessment Reports (GAR) of UNDRR (then UNISDR).

This paper aims to present the components of the landslide hazard model developed for the Flagship Report of The Coalition for Disaster Resilient Infrastructure (CDRI) to evaluate the global risk posed by earthquake- and rainfall-induced landslides to road and railway infrastructure, the latter both for the present climate regime and for future climate scenarios. The model presented in this paper (herein referred to as the GIRI landslide model) has a resolution that is about ten times greater than the GAR model, and it can be used to assess landslide probability for specific rainfall and earthquake scenarios.

2   GIRI landslide model

The GIRI model is based on the model that was originally developed by (Nadim et al. 2006) in the project "Natural disaster hotspots – a global risk report" for the World Bank (Dilley 2005) to identify the global landslide hazard and risk "hotspots". Its inputs are (i) susceptibility information and (ii) gridded information of different scenarios for each landslide-triggering factor, including rainfall and earthquake. The output consists of global scenario-based landslide hazard maps that can be used to evaluate the risk to linear infrastructure. Figure 1 shows a general flowchart of the GIRI landslide model.

In the following sections, the components of the GIRI landslide model are explained in more detail.
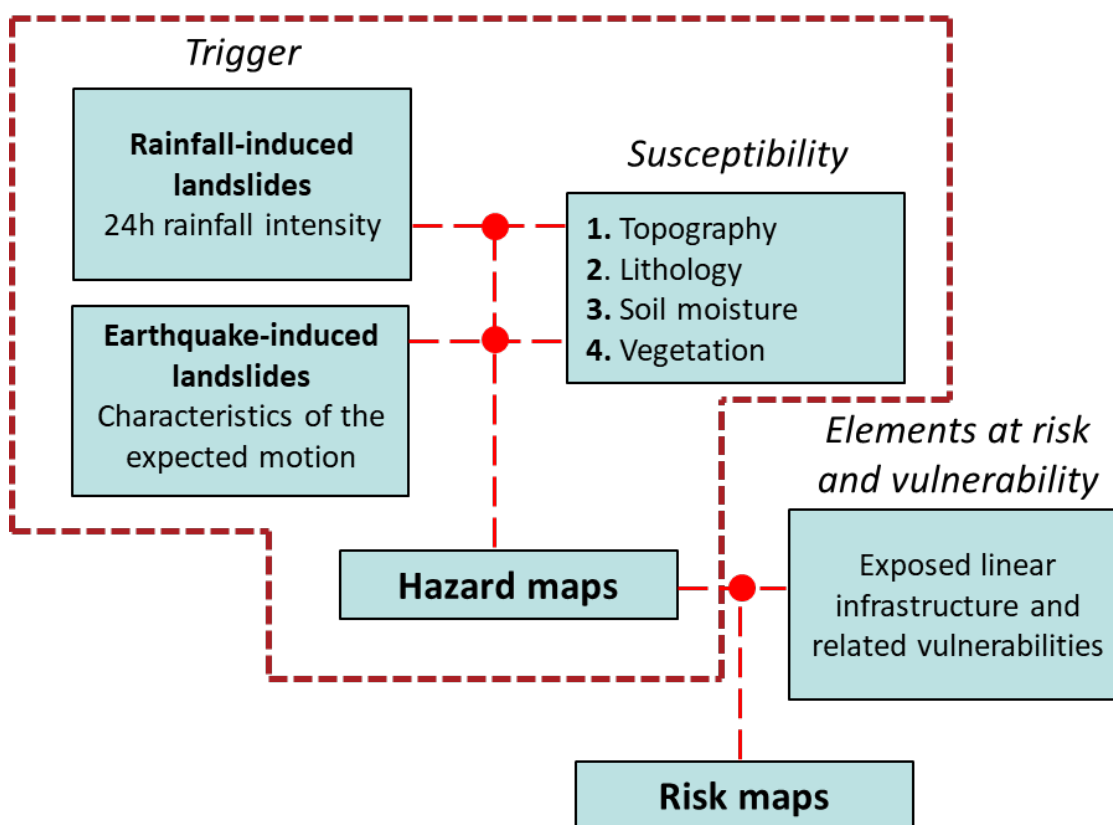

Figure 1   Flowchart of the scenario-based landslide hazard model and risk assessment for critical infrastructure.

3 Landslide susceptibility

In the GIRI landslide hazard model, the susceptibility map distinguishes landslide-prone areas. The susceptibility map has been derived by combining the information in global open-source datasets describing the topography (slope angle), lithology, vegetation, and soil moisture information (Table 1). It classifies the globe into five landslide susceptibility categories corresponding to "Very Low", "Low", "Moderate", "High", and "Very High" susceptibility. Additionally, the global landslide database for rainfall-induced landslides has been employed to visually analyse the GIRI landslide susceptibility map outputs for rainfall-induced landslides.

The following subsections introduce the input datasets used to compute susceptibility and the method applied to obtain the susceptibility factors. Then, the method to calculate the overall landslide susceptibility is explained in more detail.

Table 1 Datasets used in the GIRI landslide susceptibility model for rainfall-induced Landslides.

Type	Type of landslide	Source	Coverage	Resolution
Slope	Rainfall-induced Earthquake-induced	Derived from MERIT-Hydro DEM	Global	0.00083°≈ 90m @ equator
Lithology	Rainfall-induced Earthquake-induced	Global Lithological Map database (GLiM)	Global	Polygon data
Soil moisture	Rainfall-induced	Current climate: W5E5 Future climate: IPSL-CM6A-LR model from the ISIMIP3b data set SSP126 and SSP585 scenarios	Global	0.5°
	Earthquake-induced	ERA5 soil moisture climatology	Global	0.25°
Land cover	Rainfall-induced Earthquake-induced	ICDR Land Cover 2020	Global	0.002778°
Landslide database	Rainfall-induced	COOLR - NASA	Global	Point data

3.1   From input data to susceptibility factors

Slope factor

The slope calculation was done using the open-access software Whitebox Geospatial Analysis Tools (Whitebox GAT) developed by Lindsay (2016). The Slope tool uses the 3×3 polynomial fitting method for equal angle grids, as Florinsky (2016) and Florinsky (2017) described. The calculations are based on the spaceborne MERIT digital elevation model (DEM) by (Yamazaki et al. 2017) in a geographic coordinate system (WGS84). The pixels with DEM data are in angular units with a 3" resolution (~90 metres at the equator). The data are available as $5° \times 5°$ tiles (6000 pixels $\times$ 6000 pixels), compressed into $30° \times 30°$ packages.

Due to the large number of files (1150) and data size, the process was carried out in a series of (parallelised) Python scripts. These scripts are implemented by using Multiprocessing. It is an iterative procedure tailored towards the data structure and the parallelisation of the calculations, while the actual processing of each tile is implemented as a subclass.

The DEM was first pre-processed (mosaicked) into a single global raster containing all files using the GDAL Virtual Format to avoid edge contamination in the slope analysis. From this dataset, GDAL Translate was used to extract a new set of buffered tiles, using 5 pixels as the buffer size. The buffer size is the number of pixels multiplied by the pixel size (3 arc-seconds) measured in degrees.

The first step calculates the slope and stores the output in the same structure as the original DEM. The second step reads and transforms all layers (vegetation, lithology, moisture, and slope) into tiles with the exact resolution as the original DEM. The third step loads all the previous layers, transforming layers into susceptibility factors and calculating susceptibility. The fourth step reclassifies the susceptibility into susceptibility classes (1 to 5). The output is structured according to the same groups and tiles as the original DEM.

The slope data were then reclassified by an expert using information on landslide frequency distributions worldwide. Cells were distributed in the six different susceptibility categories (0 – 5) according to their susceptibility degree, as presented in Table 2. Intuitively, the greater the slope angle, the more susceptible the terrain is. However, since most soils have an internal friction angle smaller than 36°, slopes steeper than 36° are not likely to be covered by sediments. To account for this, the susceptibility factor for very steep slopes (steeper than 36°) has been set to decrease (see Table 2). Slopes steeper than 50° consist primarily of hard rock. It is essential

to notice that for slopes less steep than 6° (i.e., for flat or nearly flat areas), the slope factor has been set equal to zero because the resulting landslide hazard is negligible, even if all the other factors are favourable.

Table 2 Susceptibility index assigned to each slope class.

Range of slopes angle (unit: 1/100 degrees)	Classification	S_r
0000 – 600	Very low	0
601 – 1200	Low	1
1201 – 1800	Moderate	2
1801 – 2400	Medium	3
2401 – 3000	High	4
3001 – 3600	Very high	5
3601 – 4000	Probably stiff soil	4
4001 - 4400	Probably rock	3
4401 - 5000	Probably hard rock	2
> 5000	Stable hard rock	1
No Data	No Data	No Data

Lithology factor

Soil properties play a crucial role in determining slope stability. Ideally, detailed geotechnical information on the soil cover should be used to determine if the conditions for landslide initiation are met. However, only a general lithological description of the various locations is available at the global scale. Therefore, assessing the terrain susceptibility using the information available about sediment strength at the global scale has been challenging.

In this study, we have utilised the information in the Global Lithological Map database (referred to as GLiM - Hartmann and Moosdorf, 2012). GLiM was constructed by compiling existing regional geological maps, which were translated into lithological information using relevant regional literature. The database encompasses 1,235,400 polygons and employs a three-layer classification system for lithology. The first level contains 16 lithological classes comparable to previously applied definitions in global lithological maps. The two additional levels consist of 12 and 14 subclasses, offering more detailed descriptions of specific rock attributes.

For our work, we have rasterised the GLiM to match the resolution of the slope map. The information of the lithology classes and subclasses have been used to reclassify the world into three susceptibility classes (1 – 3) representing lithologies with low, moderate and high relevance for landslide susceptibility.

Soil moisture factor

Soil moisture plays a relevant role in slope stability. As water infiltrates the soil, pore pressures increase, and shear strength decreases, eventually leading to failure if the soil strength is low and the slope is steep. In the GIRI landslide susceptibility assessment for rainfall-induced landslides, rainfall data with a spatial resolution of 0.5° has been used as a proxy to assess the soil moisture conditioning factors. This method has allowed us to obtain susceptibility maps for future climate scenarios.

For 1979-2016, the W5E5 precipitation estimates (Lange 2019) have been employed. More specifically, the daily product that contains the sum of rainfall and snow water equivalent has been used to obtain the mean value of the 38 rainfall maximum monthly cumulates.

For the periods 2061-2100, the IPSL-CM6A-LR model from the ISIMIP3b data set (Frieler et al. 2017) SSP126 and SSP585 scenarios have been employed to obtain the mean of the average monthly precipitation.

The mean year maximum monthly rainfall distribution in current climate conditions has been investigated (Figure 2a). Wetter areas are generally more susceptible to rainfall-induced landslides than drier areas. This criterion has been considered to classify the mean year maximum monthly rainfall into five classes (Table 3) and assign the soil moisture susceptibility factor (S_h) accordingly.

Table 3   Soil moisture susceptibility factor assigned for each of the mean year maximum monthly rainfall categories.

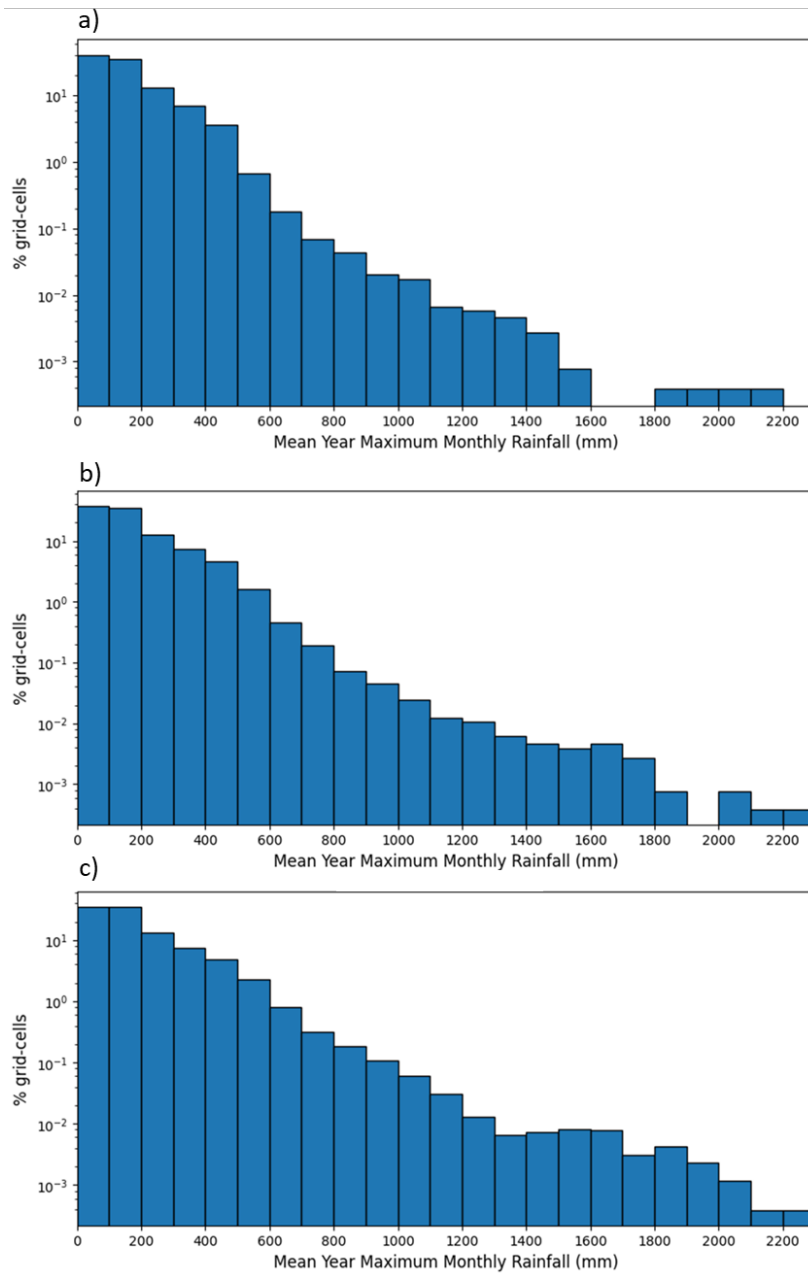| Mean Year Maximum Monthly Rainfall (MYMMR) (mm)	S_h
≤ 125	1
125 < MYMMR ≤ 250	2
250 < MYMMR ≤ 500	3
500 < MYMMR ≤ 1000	4
MYMMR > 1000	5

Figure 2   Mean year maximum monthly precipitation in (a) current climate conditions and in the period 2061-2100 with the (b) SSP126 and (c) SSP585 climate change scenarios.

Figure 2 shows the area affected by a given mean year monthly rainfall amounts for the current climate, and the two analysed future climate change scenarios (Figures 2b and 2c). As it can be observed, it is expected that the area affected by high mean year maximum monthly rainfall

amounts will slightly increase in the future. Changes in the spatial distribution of the rainfall can explain this observation.

In the future, some regions will experience higher rainfall accumulations compared to present conditions, while other areas might receive less rainfall. As a result, the overall effect is a modest increase in the mean year maximum monthly rainfall across a larger geographic area.

For the case of earthquake-induced landslides, the soil moisture information in the dataset Essential Climate Variables for assessment of climate variability from 1979 to the present (Hersbach et al. 2018) has been employed. This dataset is based on the provisional data from ECMWF's ERA5 data. Soil moisture information consists of the monthly volumetric water content climatology obtained from satellite observations in the top 7 cm of soil with a spatial resolution of 0.25°. The mean soil moisture in each pixel has been used for this work.

Table 4   Soil moisture susceptibility factor assigned for each volumetric water content category.

Volumetric water content (VWC) (m³/m³)	Susceptibility, S_h
≤ 0.16	1: Low-Moderate
0.16 < VWC ≤ 0.36	2: Moderate
0.36 < VWC ≤ 1	3: High-Very High

Vegetation factor

Vegetation can play a significant role in slope stability by providing additional cohesion to the soil and reducing soil moisture by means of evapotranspiration. Additionally, being able to distinguish between areas with vegetation cover and unvegetated areas can indicate soil availability. The C3S Land Cover v2.1 global ICDR Land Cover map for 2000 has been used (Copernicus Climate Change Service, Climate Data Store 2019; Defourny et al. 2021) in this study. The land cover map has a regular latitude-longitude grid with a 0.002778° resolution (approximately 300 m at the equator). Each pixel indicates a categorical land cover class defined using UN Land Cover Classification System classifiers.

Here, the original 38 categories from the land cover map have been re-classified using expert criteria and information contained in relevant literature into five classes with relation to non-resistance to landslides.

Table 5 Susceptibility factor for the land cover classes.

Land cover class	S_v
Bare areas	5
Sparse vegetation	4
Grassland	5
Evergreen shrubs	4
Shrubs	3
Close Forest	2
Open Forest	3
Agriculture	5
Agriculture with herbaceous cover	4
Agriculture combined with shrubs and forest	3
Water bodies	0
Permanent Ice	1
Urban areas	1

3.2   Landslide susceptibility index

The method to obtain landslide susceptibility is similar to that of Nadim et al. (2006), Nadim et al. (2013), and Jaedicke et al. (2014). Landslide susceptibility is computed as follows:

$$S = \prod_i w_i \cdot f(S_i) \tag{1}$$

where S_i are the slope, lithology, vegetation, and mean of the annual monthly rainfall factors, and w_i are the weights of the slope, lithology, vegetation and mean of the annual monthly rainfall factors, respectively. The weights of different susceptibility factors were calibrated to the information available in landslide inventories and physical processes.

More specifically, in the GIRI-model, the landslide susceptibility index is defined as:

$$S = (S_r \cdot [1 + 0.25\,(S_l - 1)] \cdot [1 + 0.25\,(S_h - 1)] \cdot S_v) \tag{2}$$

where
$$S_r = Susceptibility\ slope\ factor \in [0,\ 5]$$

$$S_l = Susceptibility\ lithology\ factor \in [1,\ 3]$$

$$S_h = Susceptibility\ soil\ moisture\ factor \in [1,\ 3]$$

$$S_v = Susceptibility\ vegetation\ factor \in [0.8,\ 1.2]$$

4   Assessment of the landslide triggering conditions

4.1   Rainfall triggering conditions

Shallow slides and debris flows are generally triggered by severe, short-duration, high-intensity rainfall events. Rainfall intensity-duration (I-D) thresholds are commonly used in regional-scale landslide early warning systems to assess the hazard a given rainfall situation represents. To determine the magnitude of a rainfall situation, the GIRI model uses 24-hour rainfall data to assess the return period of a given rainfall event.

To determine the rainfall triggering potential, the 24-hour rainfall product from the W5E5 dataset (Lange 2019) has been employed to normalise the 24-hour rainfall intensity of a given rainfall scenario as follows:

$$I_{24h-norm} = \frac{I_{24h} - \mu_{Imax}}{\sigma_{Imax}} \tag{3}$$

where I_{24h} represents the 24-hour rainfall intensity of the rainfall event, $\mu_{I_{max}}$ is the mean value of the maximum of the annual 24-hour rainfall intensity at the location of interest, and $\sigma_{I_{max}}$ represents the standard deviation of the maximum annual 24-hour rainfall intensity at the location of interest.

Table 6 shows the correspondence between $I_{24h-norm}$ and rainfall return period assuming a Gumbel distribution for the maximum annual daily rainfall at a given location. The amount of rain within 24 hours with return periods of approximately five years, 25 years, 200 years, and 1000 years have been selected as thresholds to distinguish between five rainfall hazard classes (see Fig. 3 in Section 5).

Table 6   Correspondence between $I_{24h-norm}$ and return period obtained for 24-hour rainfall intensity.

$I_{24hr-normalised}$	Return period (years)
0.72	5
1.13	10
1.86	20
2.0	23.7
2.6	50
3.1	100
3.7	200
4.4	500
4.9	1000
5.0	1087

The terrain will take a long time (decades to centuries) to adapt to a new climate regime. Therefore, for future climate scenarios, the triggering rainfall should be normalised with respect to the values of $\mu_{I_{max}}$ and $\sigma_{I_{max}}$ obtained for today's climate. This approach will capture the change in the characteristics of the triggering rainfall in the future.

4.2   Earthquake triggering conditions

The model for earthquake-triggered landslide hazard developed for the GAR reports (Nadim et al. 2013) used the peak ground acceleration (PGA) from the Global Seismic Hazard Program, GSHAP (Giardini et al. 2000; Giardini et al. 2003). The 475-year return period (10% probability of exceedance in 50 years) was employed to determine the earthquake-triggering potential in that model. Based on the calibrations done previously for the GAR model, PGA values of 0.05g, 0.15g, 0.25g, 0.35g and 0.45g have been selected as thresholds to define five seismic hazard

classes for the GIRI model (see Figure 4 in Section 5). We have considered that earthquakes with a PGA smaller than 0.05g have a negligible probability of triggering a landslide.

5 Scenario-based landslide hazard on roads and railways

The "landslide hazard index", i.e., the probability of landslide occurrence for a specific triggering event, is derived from the combination of the susceptibility index with either the rainfall or earthquake triggering conditions. The combination of the susceptibility and the rainfall-triggering conditions is done according to the hazard matrix in Figure 3.

$I_{24hr-normalised}$	Susceptibility category				
	Susc. 1	Susc. 2	Susc. 3	Susc. 4	Susc. 5
$I_{24hr-normalised} < 0.3$	~ 0	~ 0	~ 0	~ 0	~ 0
$0.3 \leq I_{24hr-normalised} < 2.0$	~ 0	~ 1	2%	3%	5%
$2.0 \leq I_{24hr-normalised} < 3.7$	~ 0	2%	3%	5%	10%
$3.7 \leq I_{24hr-normalised} < 5.0$	~ 0	3%	5%	10%	15%
$I_{24hr-normalised} \geq 5.0$	~ 0	5%	10%	15%	20%

Figure 3   Hazard matrix used to determine the probability of occurrence of a significant rainfall-induced landslide that impacts the 1km stretch of the road or railway as a function of $I_{24h-norm}$ of the precipitation scenario at that location and the Susceptibility Category.

The global (rainfall-triggered) landslide hazard index map has been integrated over rainfall events with different return periods to "translate" the combination of landslide hazard category and return period of the daily rainfall into the probability of landslide occurrence within an area.

The probabilities assigned to each hazard class have been calibrated such that the integration over all the return periods for the whole globe results in an annual number of significant rainfall-induced landslides (~400,000 globally) that is consistent with the data presented in the Global Landslide Hazard Map (The World Bank 2020).

Similarly, for earthquake-induced landslides, the susceptibility and the earthquake-triggering conditions are combined according to the hazard matrix in Figure 4. If PGA is less than 0.05g, the probability of triggering an earthquake-induced landslide is negligible, even for high susceptibility categories. The probabilities of each hazard class have been calibrated such that

the total number of significant landslides triggered by earthquakes is consistent with the approximate 130,000 landslides happening globally each year, as indicated by the World Bank report (The World Bank 2020).

PGA (g)	Susceptibility category				
	Susc. 1	Susc. 2	Susc. 3	Susc. 4	Susc. 5
0.05g ≤ PGA < 0.15g	~ 0	~ 0	~ 0	0.1%	0.5%
0.15g ≤ PGA < 0.25g	~ 0	~ 0	0.1%	0.5%	1%
0.25g ≤ PGA < 0.35g	~ 0	0.1%	0.5%	1%	5%
0.35g ≤ PGA < 0.45g	~ 0	0.5%	1%	5%	10%
PGA ≥ 0.45g	~ 0	1%	5%	10%	40%

Figure 4   Probability of occurrence of a significant earthquake-induced landslide that impacts the 1km stretch of the road or railway in question as a function of PGA of the earthquake scenario at that location and the Susceptibility Category.

To assess the hazard possessed by landslides on linear infrastructure, we have used a unit of 1km length along the road or railway and a 300 m buffer on each side of the road or railway stretch (Figure 5). The pixel with the highest susceptibility for earthquake-induced landslide in the 1km × 600m unit has been used to determine the probability of a landslide impacting the 1 km stretch of the road or railway in question (indicated in Figure 3 and Figure 4).
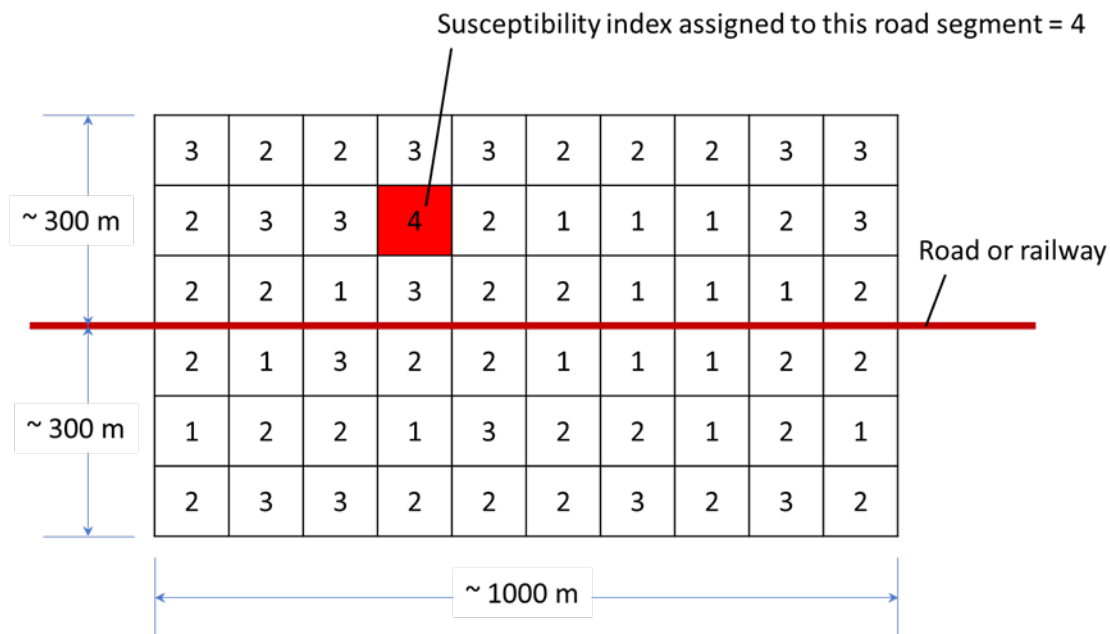
Figure 5   Schematic of buffer zones around a 1km stretch of road or railway and assigning the susceptibility index. Each box in the figure represents a pixel, and the number in the box represents the landslide susceptibility class.

6   Example results

Figure 6 shows the susceptibility map for rainfall-induced landslides obtained with the GIRI model for current climate conditions. As expected, the areas exhibiting a higher susceptibility to landslides coincide with mountainous areas with a relatively humid climate. This fact can be explained because the slope factor is relevant in susceptibility assessment.
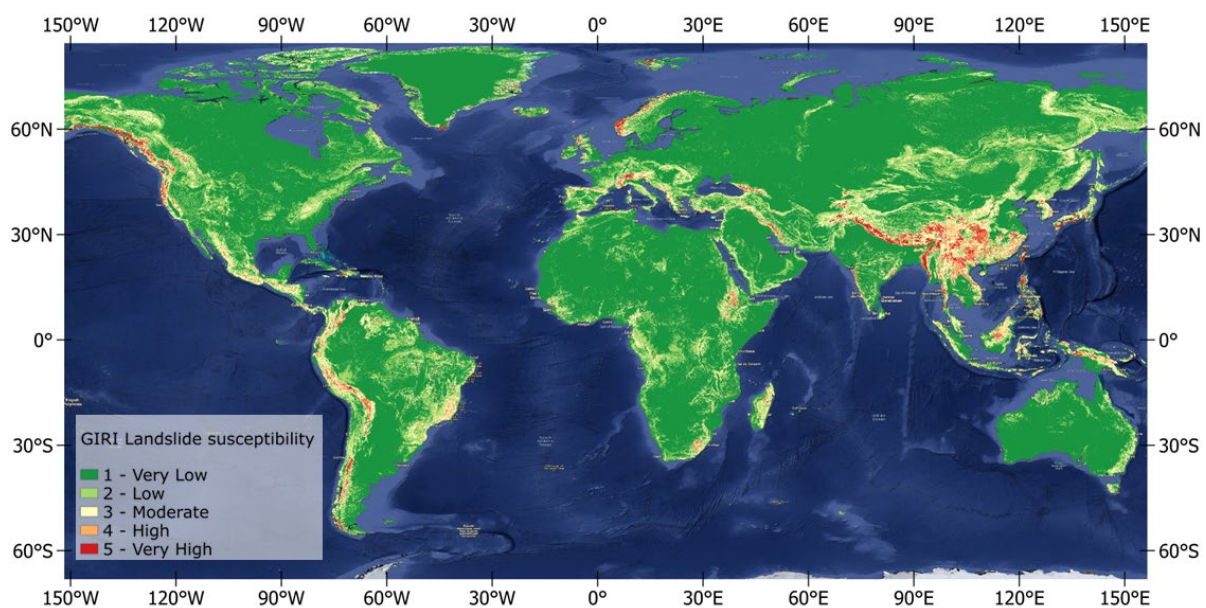
Figure 6   Susceptibility to rainfall-induced landslides obtained with the GIRI model for current climate conditions.

Evaluating the performance of landslide susceptibility maps at a global scale is challenging because of the limitations of global landslide databases. Here, the rainfall-induced landslides in the global NASA COOLR database (Juang et al. 2019) and from selected national (Ekker et al. 2013) and regional (Palau et al. 2022) inventories have been used for the visual inspection of our results for current climatic conditions. Generally, the location of the landslides coincides rather well with high-susceptibility areas. Figure 7 shows a zoom over southeast Asia. It can be observed that the regions with higher susceptibility coincide with the Himalayas, the Western Ghats, and the Zagros mountainous areas, where most landslides have been reported.
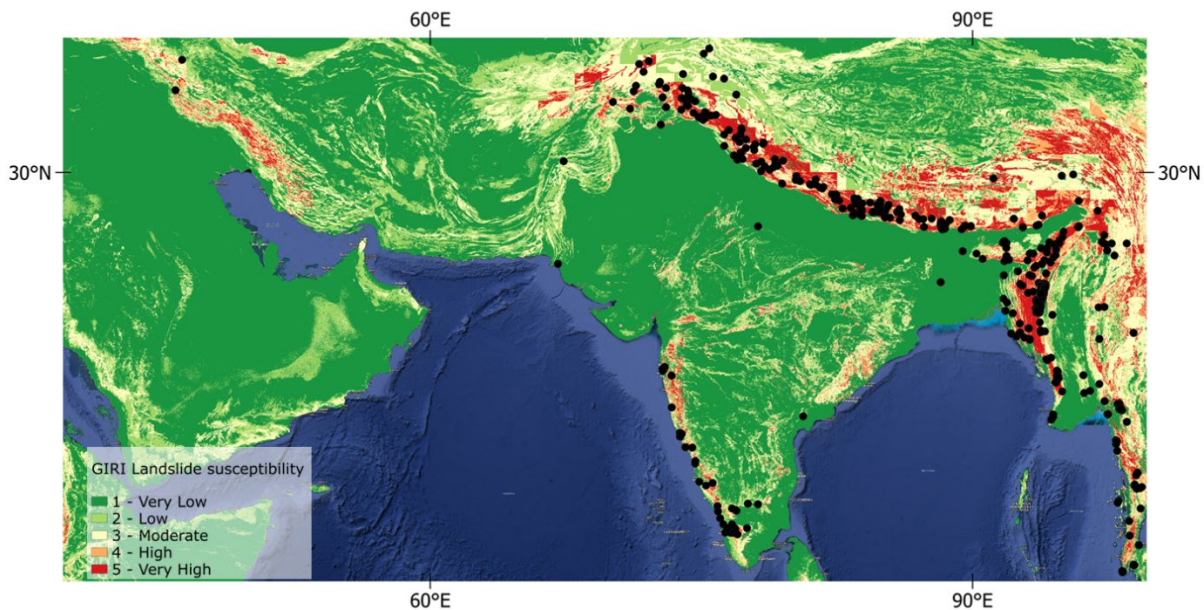
Figure 7   *Susceptibility to rainfall-induced landslides obtained with the GIRI model for current climate conditions over Southeast Asia. The Black points represent the Landslides in the NASA COOLR database (Kirschbaum et al. 2010; Juang et al. 2019).*

Landslide susceptibility maps for the present and the two analysed future climate change scenarios (Figure 8a, Figure 8b) are generally similar. However, some areas, such as the northwest of America and the southeast of Asia, exhibit a slight increase in susceptibility. This increase is larger for the SSP585 scenario than for the SSP126 scenario (Figure 8a, Figure 8b). On the other hand, our model predicts that landslide susceptibility will decrease slightly in some other areas, like Central America and the Iberian Peninsula. However, one must remember that this change in susceptibility is only due to the change in the average long-term precipitation regime. It could be the case that landslide hazard changes more dramatically if the frequency of high-intensity rainfall events decreases or increases.
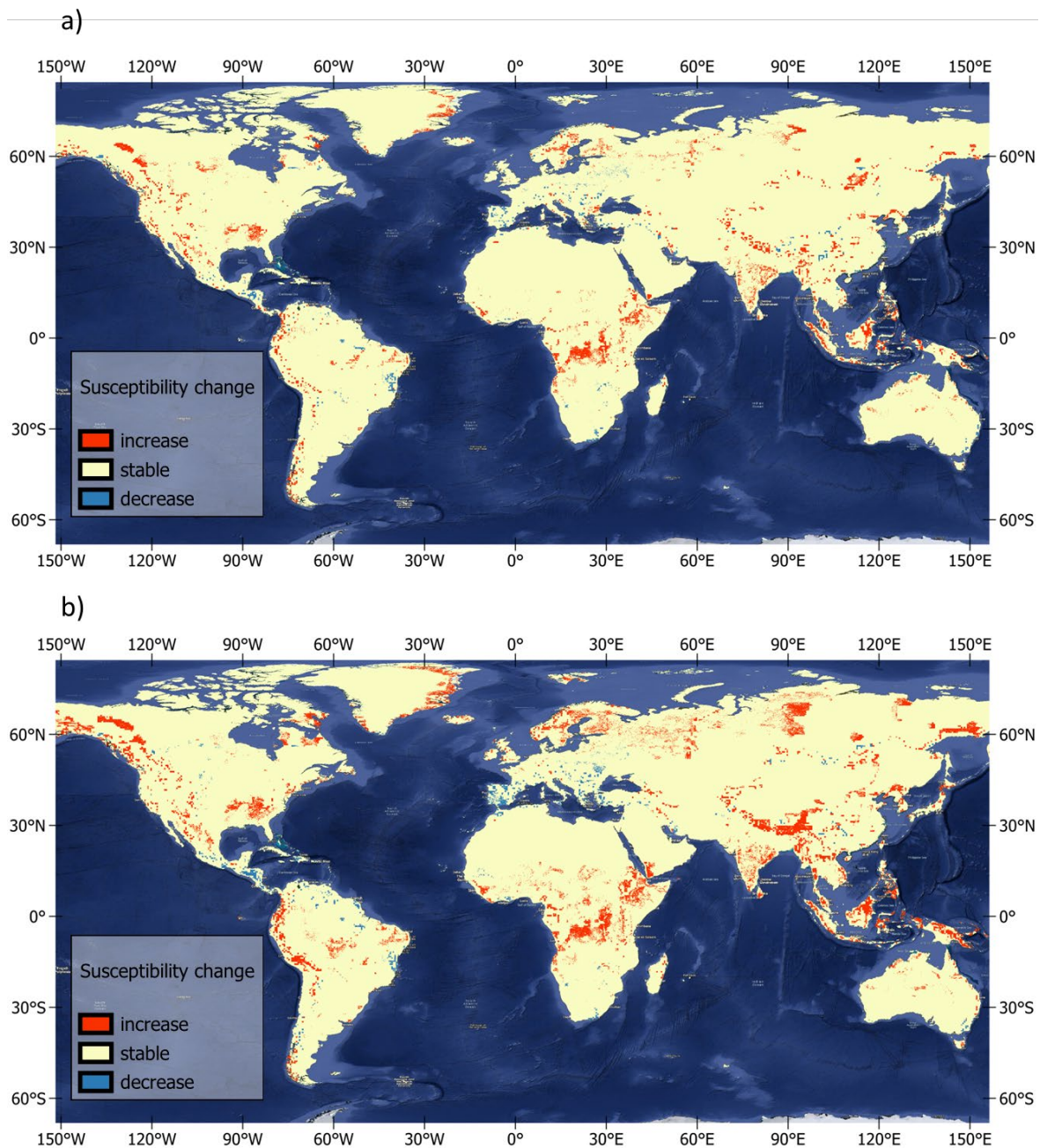
Figure 8   *(a) Difference between the susceptibility map for rainfall-induced landslides with today's climate and the susceptibility map for the future climate assuming an SSP126 scenario. (b) Difference between the susceptibility map for today's climate and future climate assuming an SSP585 scenario.*

Similarly, in the case of earthquake-induced landslides, the areas that exhibit a high susceptibility generally coincide with the locations of mountainous regions. When compared to

the susceptibility map for current climate conditions, it can be noticed that the earthquake-induced landslides susceptibility map displays a higher susceptibility in southeast Asia and western America and a lower susceptibility in western Norway. This can be explained because the soil moisture factor has a smaller weight in the model for earthquake-induced landslides. Thus, the slope angle is more relevant in determining earthquake-induced landslide susceptibility.
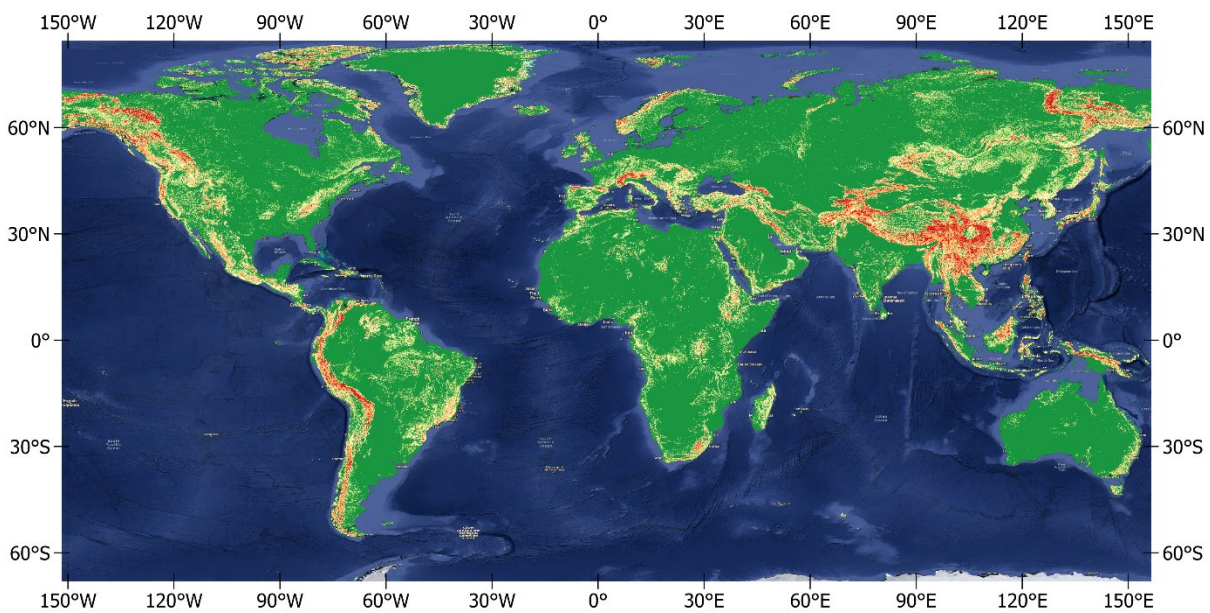

Figure 9 Susceptibility to earthquake-induced landslides obtained with the GIRI model.

7 Discussion and conclusions

A new model to probabilistically assess landslide hazard at a global scale has been developed. The GIRI landslide hazard model is used in the Flagship Report of The Coalition for Disaster Resilient Infrastructure (CDRI) to evaluate the global risk posed by landslides to road and railway infrastructure, both for the present climate regime and for future climate scenarios.

The GIRI landslide hazard model uses information on the terrain slope angle, lithology, soil moisture and vegetation to obtain a susceptibility map. Then, the susceptibility map can be combined with information on the rainfall or earthquake landslide-triggering conditions to obtain a fully probabilistic hazard map or used in a scenario-based approach with Monte Carlo simulations to assess the risk to critical infrastructure (or to other elements at risk).

The resolution of the GIRI landslide model is much higher than the resolution of the previous similar global models. This is mainly because more up-to-date datasets to describe the lithology, vegetation, soil moisture, and the terrain slope angle have been employed. In past studies (Nadim et al. 2006; Nadim et al. 2013; Jaedicke et al. 2014), a DEM with a resolution of 30 arc seconds was used. Here, we have applied a DEM with a resolution of 3 arc seconds, corresponding to approximately 90m at the equator. This has allowed a better representation of the slope angle over the world.

Another significant difference with previous models is that for the case of rainfall-induced landslides, the mean of the yearly maximum monthly precipitation has been used as a proxy to account for soil moisture preconditioning. This has allowed us to obtain susceptibility maps for the current climate conditions and future SSP126 and SSP585 climate change scenarios.

Evaluating the performance of landslide susceptibility maps has been challenging because of the limitations in global landslide inventories, which are somewhat incomplete. Generally, the areas that exhibit a higher susceptibility coincide rather well with mountainous areas where landslides have been reported in global and national landslide databases (Ekker et al. 2013; Juang et al. 2019; Palau et al. 2022).

The comparison of the susceptibility maps for rainfall-induced landslides obtained for the current climate conditions and the susceptibility maps obtained for the SSP126 and SSP585 scenarios shows a slight increase of susceptibility in some areas that will be affected by larger rainfall amounts. Susceptibility will decrease slightly in other areas, like Central America and the Iberian Peninsula. The regions where susceptibility will change in the future are larger for

the SSP585 climate change scenario Than for the SSP126 scenario. The change in landslide susceptibility predicted by the GIRI is only due to modification in the prevailing long-term precipitation patterns. Land use changes can also affect susceptibility, and landslide hazard could undergo even more pronounced changes if the frequency of occurrence of intense rainfall events rises or falls in the future.

This study analysed the hazard due to rainfall-induced and earthquake-induced landslides separately. This decision was taken mainly because the susceptibility factors for the two triggering mechanisms might be different. Additionally, the risk (to human life) due to earthquake-induced landslides is often included in the earthquake risk, and one should avoid counting the same risk twice in a multi-hazard and multi-risk context.

The rainfall-triggering conditions are based on an extreme-value analysis of 1-day precipitation instead of the extreme monthly precipitation used in the GAR model (Nadim et al. 2006; Nadim et al. 2013). The earthquake-triggering conditions are assessed in a scenario-based approach using the PGA of a simulated earthquake event at a given location.

An essential limitation of the GIRI landslide model is that it does not account for human-induced landslides. Such landslides generally have high economic consequences, such as road and railway closures, but rarely result in fatalities. Accounting for the human factor is not straightforward, as it depends on human decisions that are not easy to predict. In the future, a population density factor could be introduced to account for the increased chance of having a landslide triggered by human activity in densely populated areas.

The developed GIRI landslide hazard model enables users to obtain an event-based landslide hazard over roads and railways. The employed methodology in the GIRI model by combining susceptibility information and information on the triggering factors is very similar to the approach used in regional-scale and global-scale landslide early warning systems (Kirschbaum et al. 2009; Krøgli et al. 2018; Palau et al. 2020). However, most regional and global-scale landslide early warning systems usually adopt a qualitative or fuzzy logic approach. The GIRI landslide model output is a fully probabilistic hazard along linear infrastructures. This is relevant for risk assessment.

The susceptibility maps and hazard outputs provided by the GIRI model should only be utilised to gain a general understanding of landslide susceptibility and hazard distribution in current and future climate conditions. Due to the input parameters' limitations and our model's calibration,

the presented results cannot be applied to assess the landslide hazard at a regional scale or for urban planning.

It is not straightforward to evaluate the vulnerability of roads, railways and other transportation infrastructure components using our model. The intensity measure used for characterising landslides in physical vulnerability models is the depth and/or velocity of sediments upon impact, which are not estimated in our model. Further work needs to be done to quantify landslide magnitude at the scale of the analysis.

Acknowledgements and Funding

References

Caine N (1980) The rainfall intensity-duration control of shallow landslides and debris flows. Geografiska Annaler 62A:23–27

Copernicus Climate Change Service, Climate Data Store (2019) Land cover classification gridded maps from 1992 to present derived from satellite observation. Copernicus Climate Change Service (C3S) Climate Data Store (CDS). https://doi.org/10.24381/cds.006f2c9a

Defourny P, Lamarche C, Marissiaux Q, Brockmann C, Martin B, Kirches G (2021) Product User Guide and Specification: ICDR Land Cover 2016-2020

Dilley M (2005) Natural disaster hotspots: a global risk analysis. World Bank, Washington, D.C

Ekker R, Kværne K, Os A, Humstad T (2013) regObs - public database for submitting and sharing observations. In: International Snow Science Workshop. Grenoble, Chamonix Mont-Blanc, p 5pp

Florinsky I (2016) Digital Terrain Analysis in Soil Science and Geology - 2nd Edition, 2nd edn. Academic Press

Florinsky IV (2017) Spheroidal equal angular DEMs: The specificity of morphometric treatment. Transactions in GIS 21:1115–1129. https://doi.org/10.1111/tgis.12269

Frieler K, Lange S, Piontek F, Reyer CPO, Schewe J, Warszawski L, Zhao F, Chini L, Denvil S, Emanuel K, Geiger T, Halladay K, Hurtt G, Mengel M, Murakami D, Ostberg S, Popp A, Riva R, Stevanovic M, Suzuki T, Volkholz J, Burke E, Ciais P, Ebi K, Eddy TD, Elliott J, Galbraith E, Gosling SN, Hattermann F, Hickler T, Hinkel J, Hof C, Huber V, Jägermeyr J, Krysanova V, Marcé R, Müller Schmied H, Mouratiadou I, Pierson D, Tittensor DP, Vautard R, van Vliet M, Biber MF, Betts RA, Bodirsky BL, Deryng D, Frolking S, Jones CD, Lotze HK, Lotze-Campen H, Sahajpal R, Thonicke K, Tian H, Yamagata Y (2017) Assessing the impacts of 1.5°C global warming – simulation protocol of the Inter-Sectoral Impact Model Intercomparison Project (ISIMIP2b). Geoscientific Model Development 10:4321–4345. https://doi.org/10.5194/gmd-10-4321-2017

Froude MJ, Petley DN (2018) Global fatal landslide occurrence from 2004 to 2016. Natural Hazards and Earth System Sciences 18:2161–2181. https://doi.org/10.5194/nhess-18-2161-2018

Gariano SL, Guzzetti F (2016) Landslides in a changing climate. Earth-Science Reviews 162:227–252. https://doi.org/10.1016/j.earscirev.2016.08.011

Giardini D, Grünthal G, Shedlock K, Zhang P (2000) 74 the GSHAP global seismic hazard map. Seismological Research Letters 42. https://doi.org/10.1785/gssrl.71.6.679

Giardini D, Grünthal G, Shedlock KM, Zhang P (2003) The GSHAP Global Seismic Hazard Map. In: International Handbook of Earthquake and Engineering Seismology. Academic Press, pp 1233–1239

Guzzetti F, Peruccacci S, Rossi M, Stark CP (2008) The rainfall intensity–duration control of shallow landslides and debris flows: an update. Landslides 5:3–17. https://doi.org/10.1007/s10346-007-0112-1

Hartmann J, Moosdorf N (2012) The new global lithological map database GLiM: A representation of rock properties at the Earth surface. Geochemistry, Geophysics, Geosystems 13. https://doi.org/10.1029/2012GC004370

Jaedicke C, Van Den Eeckhaut M, Nadim F, Hervás J, Kalsnes B, Vangelsten BV, Smith JT, Tofani V, Ciurean R, Winter MG, Sverdrup-Thygeson K, Syre E, Smebye H (2014) Identification of landslide hazard and risk "hotspots" in Europe. Bulletin of Engineering Geology and the Environment 73. https://doi.org/10.1007/s10064-013-0541-0

Juang CS, Stanley TA, Kirschbaum DB (2019) Using citizen science to expand the global map of landslides: Introducing the Cooperative Open Online Landslide Repository (COOLR). PLOS ONE 14:e0218657. https://doi.org/10.1371/journal.pone.0218657

Keefer, DK (1984) Landslides caused by earthquakes. Bull. Geol. Soc. Am. 95, 406–421.

Kirschbaum DB, Adler R, Hong Y, Hill S, Lerner-Lam A (2010) A global landslide catalog for hazard applications: method, results, and limitations. Natural Hazards 52:561–575. https://doi.org/10.1007/s11069-009-9401-4

Kirschbaum DB, Adler R, Hong Y, Lerner-Lam A (2009) Evaluation of a preliminary satellite-based landslide hazard algorithm using global landslide inventories. Natural Hazards and Earth System Sciences 9:673–686. https://doi.org/10.5194/nhess-9-673-2009

Krøgli IK, Devoli G, Colleuille H, Boje S, Sund M, Engen IK (2018) The Norwegian forecasting and warning service for rainfall- and snowmelt-induced landslides. Natural Hazards and Earth System Sciences 18:1427–1450. https://doi.org/10.5194/nhess-18-1427-2018

Lange S (2019) WFDE5 over land merged with ERA5 over the ocean (W5E5)

Lindsay JB (2016) Whitebox GAT: A case study in geomorphometric analysis. Computers & Geosciences 95:75–84. https://doi.org/10.1016/J.CAGEO.2016.07.003

Nadim F, Jaedicke C, Smebye H, Kalsnes B (2013) Assessment of Global Landslide Hazard Hotspots. In: Sassa K, Rouhban B, Briceño S, McSaveney M, He B (eds) Landslides: Global Risk Preparedness. Springer, Berlin, Heidelberg, pp 59–71

Nadim F, Kjekstad O, Peduzzi P, Herold C, Jaedicke C, Kjekkstad O (2006) Global landslide and avalanche hotspots. Landslides 3:159–173. https://doi.org/10.1007/s10346-006-0036-1

Palau RM, Berenguer M, Hürlimann M, Sempere-Torres D (2022) Application of a fuzzy verification framework for the evaluation of a regional-scale landslide early warning system during the January 2020 Gloria storm in Catalonia (NE Spain). Landslides. https://doi.org/10.1007/s10346-022-01854-2

Palau RM, Hürlimann M, Berenguer M, Sempere-Torres D (2020) Influence of the mapping unit for regional landslide early warning systems: comparison between pixels and polygons in Catalonia (NE Spain). Landslides 17:2067–2083. https://doi.org/10.1007/s10346-020-01425-3

Petley D (2012) Global patterns of loss of life from landslides. Geology 40:927–930. https://doi.org/10.1130/G33217.1

The World Bank (2020) The Global Landslide Hazard Map. London, United Kingdom

Yamazaki D, Ikeshima D, Tawatari R, Yamaguchi T, O'Loughlin F, Neal JC, Sampson CC, Kanae S, Bates PD (2017) A high-accuracy map of global terrain elevations. Geophysical Research Letters 44:5844–5853. https://doi.org/10.1002/2017GL072874

Zhang, S, Zhang LM, Glade T (2014) Characteristics of earthquake- and rain-induced landslides near the epicenter of Wenchuan earthquake. Engineering Geology 175 (2014) 58-73